Study on Dynamic Behavior of Ring-Cavity Quantum-Cascade Lasers with Group Velocity Dispersion

A THESIS

SUBMITTED TO THE FACULTY OF THE GRADUATE SCHOOL

OF THE UNIVERSITY OF MINNESOTA

BY

BO WANG

IN PARTIAL FULFILLMENT OF THE REQUIREMENTS

FOR THE DEGREE OF

MASTER OF SCIENCE

Adviser: Dr. Jing Bai

Dec 2014

Acknowledgements

I would like to thank my advisor, Dr. Jing Bai, for all the help and guidance she has given me on both research and life. She genuinely cares about her students and encourages them to explore themselves.

I want to acknowledge the research support from the National Science Foundation (NSF) with Grant No. ECCS-1232273, and teaching assistantship from the Electrical Engineering department at UMD.

I also want to thank Dr. Mohammed Hasan and Dr. Debao Zhou for reviewing my thesis and serving on the defense committee.

My gratitude also goes to Dr. Khai Le for his important help with the figures of the numerical simulation work.

Thank all the fellow graduate students, faculty and staff, who make this department warm and wonderful.

Abstract

Quantum cascade lasers (QCLs) have been the common mid-infrared sources because of their high output power and agile wavelength range owing to the intersubband transitions. Previous research on QCLs shows that the instability and dynamic behaviors are more complicated than conventional semiconductor lasers due to interaction among various intracavity effects, such as material nonlinearities, unique gain and dispersions. Group velocity dispersion (GVD) plays an important role in the study of QCLs because of its effects on pulse spectrum in both unsaturation and saturation regime. To investigate the effect of group velocity dispersion in QCLs, both instability analysis and time-domain numerical simulation are presented in this thesis. A model that accounts for GVD effect and a background saturable absorber is developed based on Maxwell-Bloch equations. Stability analysis of a ring cavity QCL is performed through the linearization of dynamic equations. Depending on the results of stability analysis, the numerical simulation for time-domain pulse progression based on the split-step method is demonstrated. It is found that the instabilities of QCL with GVD are highly related to the pumping strengths, and stronger saturable absorber effect tends to make the system more stable. Numerical simulations show that Rabi side modes are enhanced by saturable absorber effect and pumping strength; GVD effect lowers the intensity of stable pulses and shrinks the pulse width. The split-step method successfully combines nonlinear and linear effects in the dynamic equations and finally leads to stable results.

Table of Contents

List of Figures and Tables

CHARPER 1

Introduction

1.1 Overview of Quantum Cascade Lasers

Quantum cascade lasers (QCLs) are semiconductor lasers in which the light is emitted based on intersubband transitions from semiconductor quantum wells. The first QCL is invented in 1994 by J. Faist *et al.* operating at cryogenic temperatures [1]. Since then this type of lasers have been developed tremendously because of its excellent design potential arising from the “band-gap engineering” related to intersubband transitions. The structure of a QCL includes alternating wells and barriers with number 500-1,000, providing a large flexibility for design (Fig. 1-1) [2]. Unlike conventional semiconductor lasers, the emission of photons is based on electronic intersubband transitions (within those injectors and active regions) instead of electron-hole recombinations [3]. This feature and the band-offsets of available semiconductor materials also make QCLs mostly work in terahertz (THz), mid-infrared (MIR) and far-infrared (FIR) regions. Now after 20 years from the first demonstration, QCLs operate in a considerably wide wavelength range from 2.6 to 400 μm [4], and can be realized in single or multiple mode, pulsed or continuous mode. So far, room temperature operation and high output power have been achieved for MIR QCLs. At room temperature the continuous wave (CW) power of ~200 W [2] and pulse power of several watts [3] have been demonstrated. In addition, MIR QCLs are often concomitant with a low-threshold current density [2]. Owing to these

advantages QCLs have become very important sources of stable mid-infrared pulses, which are desired in various applications such as high-sensitivity trace gas detection, free-space communications and infrared countermeasures [2] [5]. QCLs have also been used in plasma process monitoring and control [6].

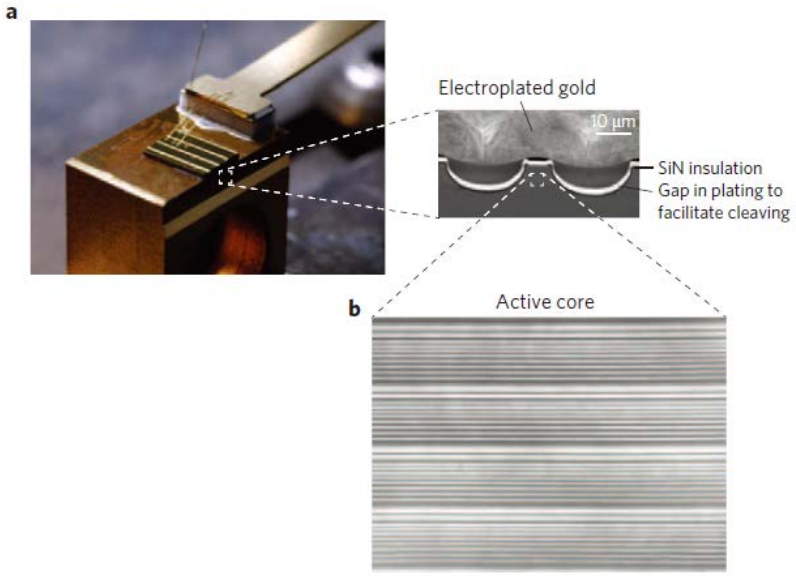

Fig. 1-1. Basic structure of a QCL. **a.** Photograph of a laser bar with four QCLs (left) and scanning electron microscopy image of the front facet of a QCL (right). **b.** High-resolution transmission electron microscopy image of a QCL, showing four periods of active regions and injectors (from Ref. 2).

Figure 1-1 shows the photographs of a typical QCL. These layers in a QCL are often grown with InGaAs/AlInAs heterojunction material system lattice matched to InP [1]. Other types also include AlGaAs/GaAs [7] and InAs/AlSb [8]. Consisting of nanometer-thick layers like above, the active regions and injectors appear alternately (i.e. one by one) in QCLs. Active regions with quantized electron motion are responsible for supplying the discrete energy states [9], photon transitions will then occur between these energy states within conduction band. The injectors however inject electrons to their adjacent active regions. Note that in QCLs an electron after

emitting a laser photon still remains in the conduction band, which means it can be reused through being injected into an adjacent active region. Then the electron emits another photon, and then collected by injectors, and so on. Hence one active region and one injector form a structure called stage, by adjusting an appropriate bias, the stages can be cascaded as an energy staircase in which photons are emitted at each of the steps [9]. The number of photons one electron can emit during traveling through the QWs is equal to the number of cascaded stages, which is the reason why QCLs are able to achieve higher emission power. This design of cascaded stages also makes QCLs essentially different from conventional semiconductor lasers, in which electrons and holes are annihilated after emitting photons. The number of stages for QCLs to work in mid-infrared spectrum ranges from 20 to 100 typically [10].

There are two common techniques of growing the periodic layers in QCLs mentioned above: molecular beam epitaxy (MBE) [11] and metal organic chemical vapor deposition (MOCVD) [12-13]. MBE is a crystal growth technique which deposits materials down to single layers of atoms. With the help of computers thickness of each layer can be precisely controlled. Therefore one can design an energy-level difference that leads to a desired emitted wavelength by adjusting the width and shapes [9]. The first QCL was fabricated by MBE [1] and MBE is still the most popular growth technique for multiple quantum wells. Compared to MBE technique, MOCVD has a faster growth rate and easier variation of composition [14], which makes it more preferred for economical mass productions. Unlike MBE which deposits crystals physically, MOCVD is a chemical vapor deposition method of

growing crystalline layers. In MOCVD the chemicals are vaporized to ultra-pure gases and then injected to reactors. Then the critical chemical reactions take place that finely dose the gases to deposit very thin layers of atoms. Ref. 12 and 13 show the examples of QCLs grown by MOCVD technique. Although it has lots of advantages, MOCVD still needs to be improved in obtaining thinner barriers and better control of interface abruptness [9], which is desired in the fabrication of long wavelength QCLs.

A typical QCL emitting diagram is shown in Figure 1-2 [15], in which the downward arrows denote the lasing transition. In this case the active region consists of three strongly coupled QWs. Electrons in ground state are rapidly injected from injectors to the active regions and turned into the upper state which is level 3. This boost is generated by the QW between injectors and active regions. Simulated laser emission then occurs relying on the transition from level 3 to level 2, which means the electron population in state 3 must exceed that in state 2. In order to achieve desired population inversion for lasing, the relaxation time for the transition from state 3 to state 2 has to exceed the electron's lifetime in state 2, which requires electrons must be extracted from state 2 as rapidly as they are injected.

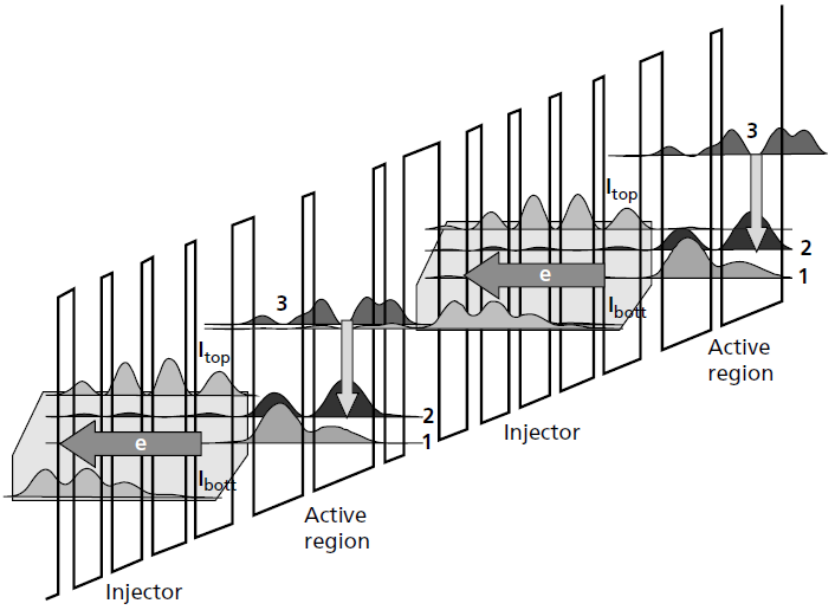

Fig. 1-2. The laser transition is indicated by the arrow between levels 3 and 2. The layer thicknesses in nanometers of one period of active material and injector are, from right to left starting from the injection barrier: 3.8/2.1/1.2/6.5/1.2/5.3/2.3/4.0/1.1/3.6/1.2/3.2/1.2/3.0/1.6/3.0. The underlined layers are n-type doped. The barriers are indicated in bold symbols; italic style shows the injector region. The applied electric field is 65 kV cm^{-1} (from Ref. 15).

This fast depopulation is achieved by designing longitudinal optical (LO) photon scattering from level 2 to level 1, which is a difference of approximately 35 meV.

In practice the above three level structure can be replaced by a superlattice to allow large current carrying capabilities [15]. The laser transition then occurs between two extended states of superlattice minibands. A so-called bound-to-continuum transition also exists in the case of transition between a localized state and an extended superlattice state. Besides vertical transitions as shown in Fig. 1-2, the transition can also be diagonal, which increases the upper-laser-state life time [15].

Laser action requires that the material gain overcomes the device losses. The material gain coefficient of QCL can be expressed as [16]

$$g = \tau_3 \left(1 - \frac{\tau_2}{\tau_{32}}\right) \frac{4\pi e z_{32}^{\ 2}}{\lambda \varepsilon_0 n_{ef} L_p} \frac{1}{2\gamma_{32}} \tag{1-1}$$

where τ_3 and τ_2 are the total life time in level 3 and level 2 respectively, τ_{32} is the relaxation time of transition from 3 to 2, z_{32} is the matrix dipole moment for 3-2 transition, n_{ef} is the effective refractive index at wavelength λ, L_p is the thickness of one active region and injector, ε_0 is the vacuum dielectric constant, e is elementary charge, and $2\gamma_{32}$ is the full width at half maximum of the luminescence spectrum.

There are two main losses [15] in QCL: one is the non-resonant free-carrier losses in the waveguide, α_w, typically calculated with a Drude model; the other one is mirror losses, α_m, calculated by $\alpha_m = (1/L)\ln(R)$, where R is the mirror reflectivity.

The threshold current density J_{th} is then given by [15]

$$\frac{\alpha_m + \alpha_w}{g\Gamma} \tag{1-2}$$

where Γ is the confinement factor with a typical order of 0.5.

For the QCL in Fig. 1-2, the losses can be estimated [15] as $\alpha_m = 5.1 cm^{-1}$ and $\alpha_w = 19 cm^{-1}$, leading to a threshold current density of $J_{th} = 1.6 kA/cm^2$. This reflects one of the main limitations of QCLs, i.e. high threshold and operating currents.

1.2 Dynamic Behaviors of QCLs

In addition to the conventional nonlinearities of semiconductor lasers, the dynamics of QCL is also affected by its typical ultrafast gain recovery and carrier

lifetime (on the order of picoseconds) due to the intersubband transitions discussed before. The combination of optical nonlinearities and ultrafast dynamics makes it much more complicated and interesting to analyze the behaviors of QCL.

Self-Mode-Locking (SML) is the technique normally used to generate picosecond and femtosecond duration laser pulses in traditional semiconductor lasers. In semiconductor lasers SML is commonly achieved by saturable absorber (SA) effect that originates from the Kerr nonlinearity [17]. In the case of Kerr nonlinearity presents, the refractive index can be approximated by $n = n_0 + n_2 I$, where n_0 is the linear refractive index, n_2 is the nonlinear refractive index, and I is the light intensity in medium. With n_2 be positive, any pulse propagating in Kerr nonlinear medium will have a highest refractive index in the peak since the intensity is highest, in both transverse and longitudinal directions. In the transverse direction, this leads to an increase of beam confinement at the center and a narrower beam diameter, which induces decreased waveguide loss [9]. This kind of decreasing optical loss with increasing intensity is the saturable absorber effect mentioned above, it is hence sometimes called transverse Kerr effect. Along with saturable absorber effect, Kerr nonlinearity also causes the longitudinal Kerr effect, which induces self-phase-modulation (SPM) of lasers. SPM is known that can broaden the frequency spectrum and concurrently shorten the pulse duration [17]. With the saturable absorber stabilizes the mode-locked pulses and SPM shapes the pulse as chirped and further compresses the pulse [9], one can achieve short laser pulses in Kerr medium.

Ref. 18 reported the generation of picosecond self-mode-locked pulses from

MIR QCLs at the cavity round-trip frequency. The pulses generated in a 3.5-mm-long 8-μm QCL at 80K are shown in Fig. 1-3, as well as a photocurrent that is sharp feature centered at the laser round-trip frequency.

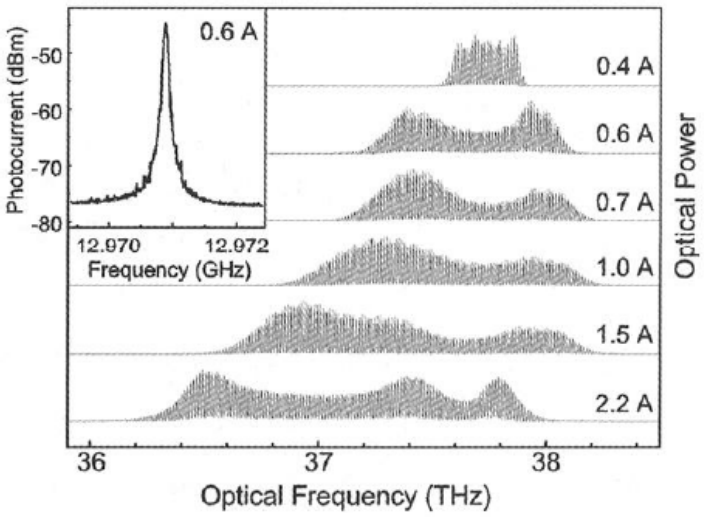

Fig. 1-3. Optical spectra of QCL with different biases. Inset: Microwave spectrum of the photocurrent generated by the same laser (from Ref.18).

The SML in transverse directions are essentially related to saturable absorber caused by Kerr nonlinearity. An extremely broad multimode spectrum is also observed in Fig. 1-3, this large frequency broadening was interpreted by SPM theory in their work. However later studies on ultrashort pulses generation of QCLs show that the SML is actually not dominated by saturable absorber [19] like conventional lasers due to the ultrafast gain recovery. Instead a coherent Risken-Nummedal-Graham-Haken (RNGH)[20] [21] like instability is proposed for the mode locking. For instance, in Ref. 22 the optical spectrum of a 3 μm wide QCL emitting at 8.38 μm is presented as shown in Fig. 1-4. The threshold of the instability j is can be just a few tens percent larger than the laser threshold j_{th} discussed before. And Fig. 1-5 illustrated that the separation between the two sidebands is about twice the Rabi frequency. These behaviors are similar to coherent RNGH instability.

As mentioned before, this property is caused by fast gain recovery of QCL, which eliminates relaxation oscillations in the transient response. With intensity getting larger the Rabi frequency is faster than the dephasing rate the electron transition is strongly coherent [9].

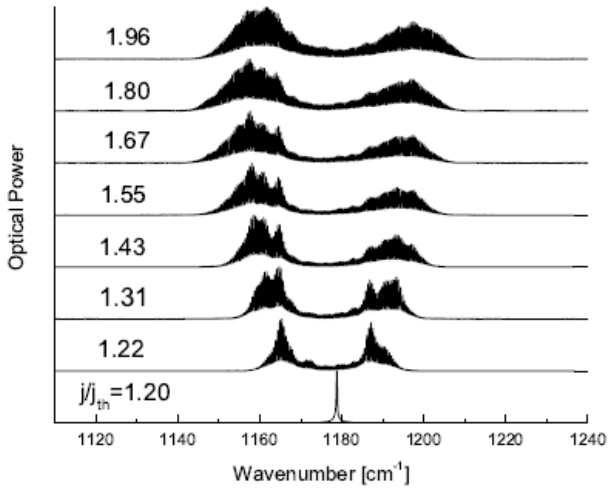

Fig. 1-4. Optical spectra vs. pumping ratio (j / j_{th}) above threshold obtained at 300K (from Ref.22).

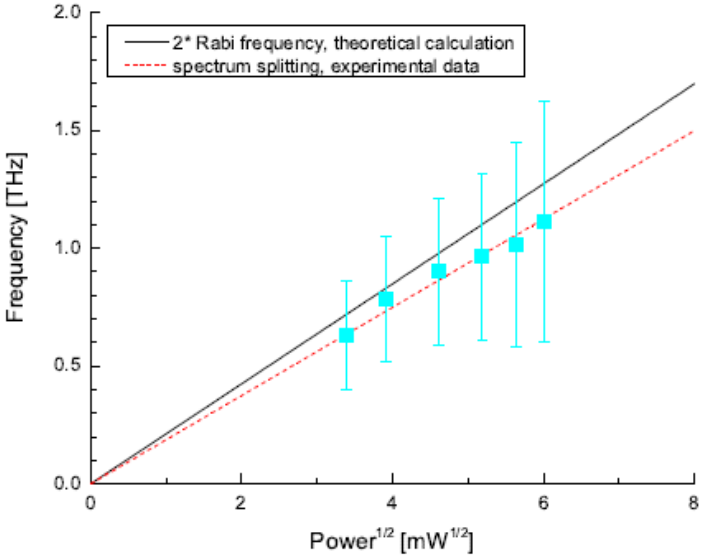

Fig. 1-5. Spectral splitting and twice the Rabi frequency vs. square root of output power collected from a single laser facet (from Ref.22).

Here Rabi frequency is the frequency in which oscillation occurs in a QCL system. In QCL this sort of RNGH like instability has two main differences from the

original instability, one is lower instability threshold, and the other one is the missing central mode. Saturable absorber effect, however, is responsible for the lower threshold in this case. The missing of central mode may be caused by the combination of saturable absorber and spatial hole burning (SHB). In Ref. 23 a model that can account for coherent phenomena, a saturable absorber and SHB is developed for multimode regimes in QCLs. Their theoretical work on SHB agrees with the experimental results, and concludes that inclusion of SHB generates expected spectra which is missing central mode.

1.3 Motivations

Besides the nonlinearities in laser medium, dispersive effects also affect the spectrum and pulse shape since QCLs are generating short pulses. Group velocity dispersion (GVD) is just an important one due to its effects on pulse spectrum in both unsaturation and saturation regime [24]. For QCLs it is even more interesting since the combination of Kerr nonlinearity and gain dispersion in lasing medium [25]. The GVD in QCLs is embedded in the same structure with Kerr nonlinearity, and both of them originate from the intersubband transitions between quantum wells. There has been some work on the effects of GVD. A time domain upconversion measurements of GVD in an active mid-infrared QCL is presented in [26]. It is shown that the estimated total GVD is in the negative dispersion regime and a maximum $\beta 2 \sim -4.6 \times 10^{-6}$ ps2/μm is observed at the 5 μm peak gain transition [26]. Ref. 27 reports self-induced transparency (SIT) modelocking of QCLs under GVD and saturable

absorber can be obtained with their magnitudes below critical limits. The effects of GVD on the stability of QCLs for Fabry-Perot QCLs are also investigated in [28]. However there has not been the investigation into the effects of GVD and saturable absorber on the pulse propagation for QCLs. In this thesis, we are trying to perform a complete simulation on stability and pulse progress of MIR QCLs by accounting for both GVD and saturable absorber effect. To avoid the complexity brought by the SHB effect, we will build our model based on ring-cavity QCLs instead of Fabry-Perot cavity. Our work is organized as follows: in Chapter 2 a detailed stability analysis of QCL including a saturable absorber and GVD is demonstrated and the results are discussed; Chapter 3 presents numerical simulations based on stability analysis using split-step method; Chapter 4 provides the conclusion and discusses future recommendations.

CHARPER 2

Stability Analysis of Ring-QCLs with Group Velocity Dispersion and Saturable Absorber Effect

2.1 Background

Linear stability analysis is often used to investigate whether a system becomes stable when time approaching infinity. The stability analysis of Fabry-Perot QCLs has been investigated thoroughly in Ref. [28]. In this chapter, we apply the similar analysis procedures to ring-cavity QCLs.

The structure of ring-QCL laser is shown in Figure 2-1, where R indicates the reflectivity of a mirror, and arrows denote the light propagation direction. As the name indicates, light in a ring-cavity QCL makes a round trip through the cavity.

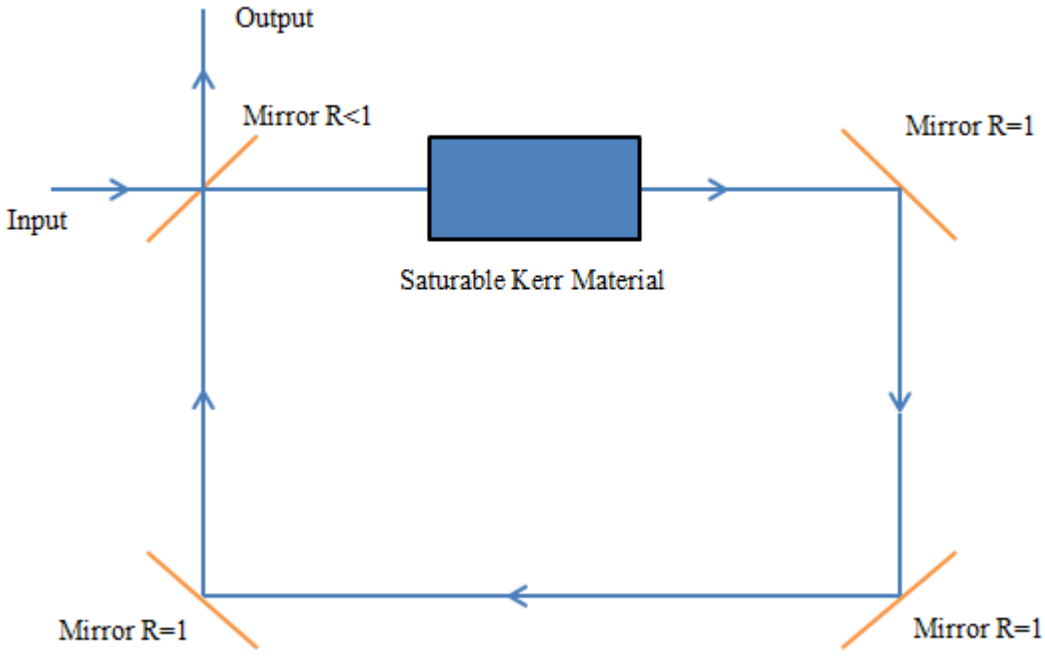

Fig. 2-1. Light propagation in a ring-cavity QCL.

To understand the linear stability analysis principals, consider the following time-vary system for example:

$$\begin{aligned} \dot{x} &= f(x, y) \\ \dot{y} &= g(x, y) \end{aligned} \tag{2-1}$$

A steady state $(\overline{x}, \overline{y})$ is time independent so that

$$\begin{aligned} f(\overline{x}, \overline{y}) &= 0 \\ g(\overline{x}, \overline{y}) &= 0 \end{aligned} \tag{2-2}$$

Consider a small perturbation from the steady state as

$$\begin{aligned} x &= \overline{x} + u \\ y &= \overline{y} + v \end{aligned} \tag{2-3}$$

where u and v are understood to be small. The question of interest becomes that whether u and v will decay to zero or not with time approaching infinity. If so then the system is called to be stable, if not the system is considered unstable. In a stable case x and y change towards the steady state mentioned above.

To investigate the change of u and v, the differential equations of them have to be derived. Substituting Eq. (2-3) to Eq. (2-1) we have

$$\begin{aligned} \dot{u} &= R(\overline{x}, \overline{y})u + S(\overline{x}, \overline{y})v \\ \dot{v} &= H(\overline{x}, \overline{y})u + Q(\overline{x}, \overline{y})v \end{aligned} \tag{2-4}$$

$\overline{x}, \overline{y}$ only exist in the coefficients of u and v since $f(\overline{x}, \overline{y}) = 0$ and $g(\overline{x}, \overline{y}) = 0$. Rewrite Eq. (2-4) into matrix form

$$\begin{bmatrix} \dot{u} \\ \dot{v} \end{bmatrix} = \begin{bmatrix} R(\overline{x}, \overline{y}), S(\overline{x}, \overline{y}) \\ H(\overline{x}, \overline{y}), Q(\overline{x}, \overline{y}) \end{bmatrix} \begin{bmatrix} u \\ v \end{bmatrix} \tag{2-5}$$

Eq. (2-5) describes the evolution of perturbations u and v, and the matrix is called Jacobian matrix of the system at steady state.

The stability of original system is determined by eigenvalues of Jacobian matrix

as follows [29]: if all the eigenvalues of the Jacobian matrix have real parts less than zero, then the steady state is stable; if at least one of the eigenvalues has a positive real part, then the steady state is unstable; otherwise there is no conclusion.

The above method of stability analysis is used in the following sections, with some modifications based on the actual equations we derive.

2.2 Linear Stability Analysis with Saturable Absorber and GVD

The model for our work is derived from the Maxwell-Bloch equations [29] in a two level gain medium. We consider a ring cavity here, SHB is not presented because there are no standing waves in the cavity [23]. The GVD is accounted as a second-order term, and a saturable absorber is also included as follows:

$$\frac{\partial E}{\partial t} = \frac{c}{n}\left[-\frac{\partial E}{\partial z} - P - \frac{1}{2}(l_0 - \hat{\gamma} \mid E \mid^2)E - \frac{1}{2} i\beta_2 \frac{\partial^2 E}{\partial t^2} \right] \tag{2-6}$$

$$\frac{\partial P}{\partial t} = -\frac{1}{2}\sigma E - \frac{P}{T_2} \tag{2-7}$$

$$\frac{\partial \sigma}{\partial t} = \frac{l_0 p_r}{T_1 T_2} - \frac{\sigma}{T_1} + (E^* P + E P^* + c.c.) \tag{2-8}$$

where E, P and σ represent the normalized[8] electrical filed, polarization and average population inversion in QCL lasing medium respectively. The token * and c.c. in Eq. (2-8) represent the complex conjugates. T_1 and T_2 are the longitudinal and transverse relaxation times. l_0 is the linear loss in cavity; $\hat{\gamma}$ is often called self-amplitude modulation coefficient[11] and expressed as $\hat{\gamma} = \gamma \hbar^2 / \mu^2$, where γ is the coefficient characters the strength of saturable absorber and μ is the transition dipole moment.

p_r is pumping above lasing threshold. Finally β_2 is the GVD coefficient.

To perform the linearization of the Eq. (2-6)-(2-8), we assume the variables contain a steady state value and a small perturbation:

$$E(z,t) = \bar{E}(z) + \delta E(z,t) \tag{2-9}$$

$$P(z,t) = \bar{P}(z) + \delta P(z,t) \tag{2-10}$$

$$\sigma(z,t) = \bar{\sigma}(z) + \delta\sigma(z,t) \tag{2-11}$$

where δ indicates the perturbation. Substituting expression (2-9)-(2-11) to Eq. (2-6)-(2-8) induces the steady state equations which have the solutions:

$$\bar{\sigma} = \frac{1}{T_2}(l_0 - \hat{\gamma}\bar{E}^2) \tag{2-12}$$

$$\bar{P} = -\frac{1}{2}(l_0 - \hat{\gamma}\bar{E}^2)\bar{E} \tag{2-13}$$

$$(l_0 - \hat{\gamma}\bar{E}^2)(1 + T_1 T_2 \bar{E}^2) = l_0 p_r \tag{2-14}$$

and a set of equations with respect to the perturbations:

$$\frac{n}{c}\frac{\partial\delta E}{\partial t} + \frac{\partial\delta E}{\partial z} = -\delta P - \frac{1}{2}\left(l_0 - 3\hat{\gamma}\,|\,\bar{E}\,|^2\right)\delta E - \frac{i\beta_2}{2}\frac{\partial^2\delta E}{\partial t^2} \tag{2-15}$$

$$\frac{\partial\delta P}{\partial t} = -\frac{1}{2}(\bar{E}\delta\sigma + \bar{\sigma}\delta E) - \frac{\delta P}{T_2} \tag{2-16}$$

$$\frac{\partial\delta\sigma}{\partial t} = -\frac{\delta\sigma}{T_1} + 2\bar{E}\delta P + 2\bar{P}\delta E \tag{2-17}$$

In order to separate the instabilities on amplitude and phase, we rewrite the variables to polar form i.e. $X(z,t) = [\bar{\rho}(z) + \delta\rho(z,t)]\exp[j\bar{\theta}(z) + j\delta\theta(z,t)]$, where X represents E, P or σ, ρ indicates amplitude, and θ indicates phase.

Using approximation $e^{j\delta\theta} \approx 1 + j\delta\theta$ and $X(z,t) = \bar{X}(z) + \delta X(z,t)$ one has expression

$$\delta X(z,t) = [\delta\rho(z,t) + j\bar{\rho}(z)\delta\theta(z,t)]e^{j\bar{\theta}(z)} \tag{2-18}$$

After apply the above expression for E, P and σ, one gets the amplitude stability equations

$$\frac{n}{c}\frac{\partial\delta\rho^E}{\partial t} + \frac{\partial\delta\rho^E}{\partial z} = -\delta\rho^P - \frac{1}{2}\left(l_0 - 3\hat{\gamma}\,|\,\bar{E}\,|^2\right)\delta\rho^E - \frac{i\beta_2}{2}\frac{\partial^2\delta\rho^E}{\partial t^2} \tag{2-19}$$

$$\frac{\partial\delta\rho^P}{\partial t} = -\frac{1}{2}(\bar{E}\delta\rho^\sigma + \bar{\sigma}\delta\rho^E) - \frac{\delta\rho^P}{T_2} \tag{2-20}$$

$$\frac{\partial\delta\rho^\sigma}{\partial t} = -\frac{\delta\rho^\sigma}{T_1} + 2\bar{E}\delta\rho^P + 2\bar{P}\delta\rho^E \tag{2-21}$$

and equations indicate phase instabilities

$$\frac{n}{c}\bar{\rho}^E\frac{\partial\delta\theta^E}{\partial t} + \bar{\rho}^E\frac{\partial\delta\theta^E}{\partial z} = -\bar{\rho}^P\delta\theta^P - \frac{1}{2}\left(l_0 - 3\hat{\gamma}\,|\,\bar{E}\,|^2\right)\bar{\rho}^E\delta\theta^E - \frac{i\beta_2}{2}\bar{\rho}^E\frac{\partial^2\delta\theta^E}{\partial t^2} \tag{2-22}$$

$$\bar{\rho}^P\frac{\partial\delta\theta^P}{\partial t} = -\frac{1}{2}(\bar{E}\bar{\rho}^\sigma\delta\theta^\sigma + \bar{\sigma}\cdot\bar{\rho}^E\delta\theta^E) - \bar{\rho}^P\frac{\delta\theta^P}{T_2} \tag{2-23}$$

$$\bar{\rho}^\sigma\frac{\partial\delta\theta^\sigma}{\partial t} = -\bar{\rho}^\sigma\frac{\delta\theta^\sigma}{T_1} + 2\bar{E}\bar{\rho}^P\delta\theta^P + 2\bar{P}\bar{\rho}^E\delta\theta^E \tag{2-24}$$

where ρ^E and θ^E represent amplitude and phase of electrical field respectively, same for P and σ. Eq. (2-19)-(2-21) and Eq. (2-22)-(2-24) imply the instabilities of amplitude and phase respectively. In next section we present the stability analysis based on these two sets of equations.

2.3 Stability Analysis solving Quadratic Eigenvalue Problem

The stability of the system is determined by the eigenvalues of Eq. (2-19)-(2-21) and Eq. (2-22)-(2-24). However the second order term of GVD induces the quadratic eigenvalue problem that needs to pay attention to. Quadratic eigenvalue problem

degrades to a standard eigenvalue problem if one transforms the second order differential equation to a first order differential equation. We take Eq. (2-19)-(2-21) of amplitude stability as an example of addressing this problem.

In detail, an extra variable $\partial\delta\rho^E/\partial t$ is defined so that the equation set can be linearized to the matrix form as:

$$\frac{\partial}{\partial t}\begin{bmatrix}\frac{\partial\delta\rho^E}{\partial t}\\ \delta\rho^E\\ \delta\rho^P\\ \delta\rho^\sigma\end{bmatrix}=\begin{bmatrix} i\frac{2n}{c\beta_2} & \frac{2i}{\beta_2}\left[\frac{\partial}{\partial z}+\frac{1}{2}\left(l_0-3\hat{\gamma}\,|\bar{E}|^2\right)\right] & \frac{2i}{\beta_2} & 0\\ 1 & 0 & 0 & 0\\ 0 & -\frac{1}{2}\bar{\sigma} & -\frac{1}{T_2} & -\frac{1}{2}\bar{E}\\ 0 & 2\bar{P} & 2\bar{E} & -\frac{1}{T_1}\end{bmatrix}\begin{bmatrix}\frac{\partial\delta\rho^E}{\partial t}\\ \delta\rho^E\\ \delta\rho^P\\ \delta\rho^\sigma\end{bmatrix} \quad (2\text{-}25)$$

The eigenvalues of the matrix in equation (2-25) describe the stability of amplitude. Suppose λ is any of the eigenvalues, after some mathematical manipulations we have

$$\frac{d\delta\rho^E(z)}{dz}=f(\lambda)\delta\rho^E(z) \quad (2\text{-}26)$$

where

$$f(\lambda)=-i\frac{\beta_2}{2}\lambda^2-\frac{n}{c}\lambda-\frac{1}{2}\left(l_0-3\hat{\gamma}\,|\bar{E}|^2\right)+\frac{\bar{\sigma}T_2+2\bar{P}\bar{E}T_1T_2}{2\left[\left(T_1+\lambda T_1T_2\right)\left(T_2+\lambda T_1T_2\right)+\bar{E}^2T_1T_2\right]} \quad (2\text{-}27)$$

Therefore in a ring cavity with length L there is

$$\delta\rho^E(L)=\delta\rho^E(0)e^{f(\lambda)L} \quad (2\text{-}28)$$

Because we are considering a ring cavity, where the light propagate to the end then start as the initial pulse again. Thus on the two boundaries z=0 and z=L, the electrical field is assumed to be the same, that is

$$\delta\rho^E(0)=\delta\rho^E(L) \quad (2\text{-}29)$$

Substituting Eq. (2-29) to Eq. (2-28) leads to

$$f(\lambda_k) = j\frac{2\pi k}{L} \tag{2-30}$$

where λ_k are the eigenvalues, and k is any integer number i.e. 0, ±1, ±2, …

Here each integer number k represents a transverse wave mode with an offset frequency Δf from the central frequency f_0, and $\Delta f = (c/nL)k$, which implies that the difference between two adjacent wave modes is the round trip frequency along the cavity [28]. The eigenvalues of Eq. (2-25) λ_k indicate the stabilities of amplitude in different modes. For each mode, if the maximum real part of all the eigenvalues is negative, the mode is stable; if it is zero, the mode is marginally stable; and if it is positive, the mode is unstable [29].

For the phase instabilities, we derive the equation set (2-31) similarly. It can be proved that its eigenvalues are the same with the amplitude one, which is Eq. (2-25). Thus the amplitude and phase instabilities can be summarized in one, which is presented in section of results and discussions.

$$\frac{\partial}{\partial t}\begin{bmatrix} \frac{\partial \delta\theta^E}{\partial t} \\ \delta\theta^E \\ \delta\theta^P \\ \delta\theta^\sigma \end{bmatrix} = \begin{bmatrix} i\frac{2n}{c\beta_2} & \frac{2i}{\beta_2}\left[\frac{\partial}{\partial z} + \frac{1}{2}\left(l_0 - 3\hat{\gamma}\,|\,\bar{E}\,|^2\right)\right] & \frac{2i}{\beta_2}\frac{\bar{\rho}^P}{\bar{\rho}^E} & 0 \\ 1 & 0 & 0 & 0 \\ 0 & -\frac{1}{2}\bar{\sigma}\frac{\bar{\rho}^E}{\bar{\rho}^P} & -\frac{1}{T_2} & -\frac{1}{2}\bar{E}\frac{\bar{\rho}^\sigma}{\bar{\rho}^P} \\ 0 & 2\bar{P}\frac{\bar{\rho}^E}{\bar{\rho}^\sigma} & 2\bar{E}\frac{\bar{\rho}^P}{\bar{\rho}^\sigma} & -\frac{1}{T_1} \end{bmatrix} \begin{bmatrix} \frac{\partial \delta\theta^E}{\partial t} \\ \delta\theta^E \\ \delta\theta^P \\ \delta\theta^\sigma \end{bmatrix} \tag{2-31}$$

2.4 Results and Discussions

To investigate the GVD in a practical structure, we chose the ~5μm QCL (D3281) used in [26] as our prototype of the study. This is an InGaAs/InalAs based QCL grown by metal-organic vapor phase epitaxy (MOVPE), we take its measured value

of β_2 = -4.6 × 10^{-6} $ps^2/\mu m$ as our base value β_0. Since the design of the QCL (wafer No. 3251) in [23] is similar, we can adopt the other parameters such as saturable absorber coefficient. We take the base value of saturable absorber coefficient as $\gamma_0=10^{-9}$ cm/V^2. Other parameters used are listed in table 2-1.

Quantity	Symbol	Value
Gain recovery time	T_1	0.5 ps
Dephasing time	T_2	0.067 ps
Linear cavity loss	l_0	7 cm^{-1}
Transition dipole element	μ	2.54 nm×e
Background refractive index	n	3.25
Cavity length	L	6 mm

Table 2-1. The Parameter used in stability analysis.

As mentioned before, the amplitude and phase instabilities in ring cavity can be illustrated as one. We present the stability analysis results with changing pumping strengths as well as GVD and saturable absorber in Fig. 2-2, which shows stability plot with the presence of GVD and saturable absorber under different pumping strengths: (2-2A) $p_r = 2$, (2-2B) $p_r = 3$, (2-2C) $p_r = 4$, (2-2D) $p_r = 6$. All the graphs in Fig. 2-2 have the same inset of line definition as that in (2-2A). The $\delta\omega/2\pi$ represents different frequency offsets from the central frequency, i.e. $\delta\omega/2\pi = 0$ indicates central frequency itself. These frequencies are determined by the number of round trips along the cavity. And parametric gain is the largest real part of all eigenvalues of the Jacobian matrix, which indicates the instability.

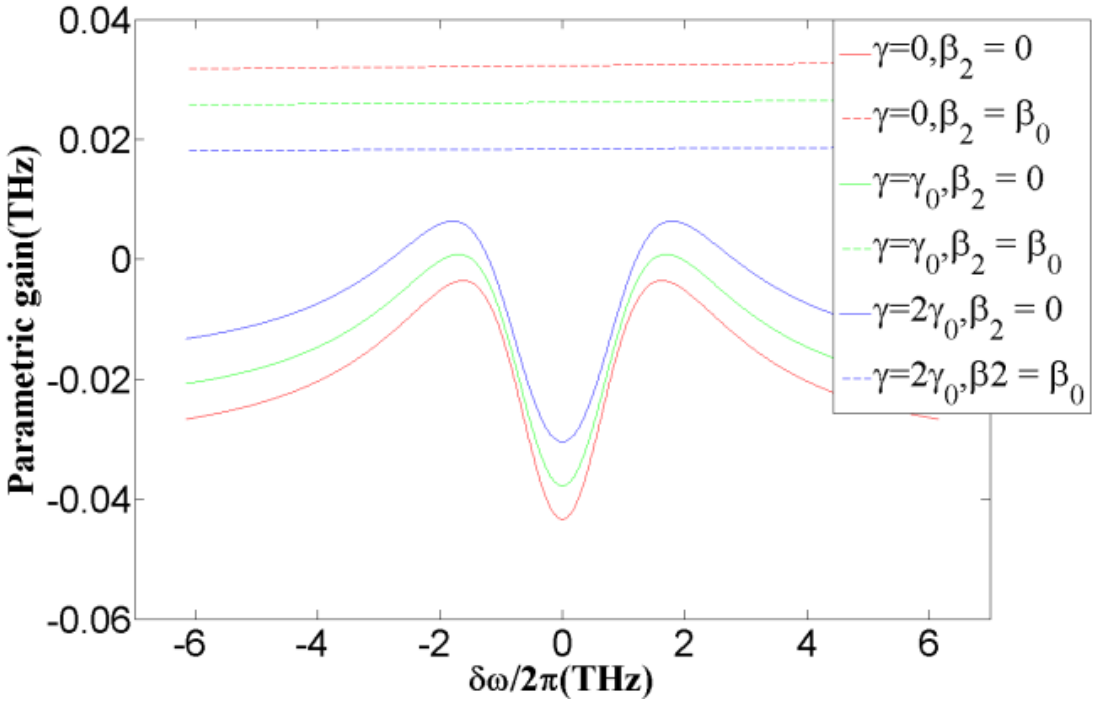

Fig. (2-2A). $p_r = 2$.

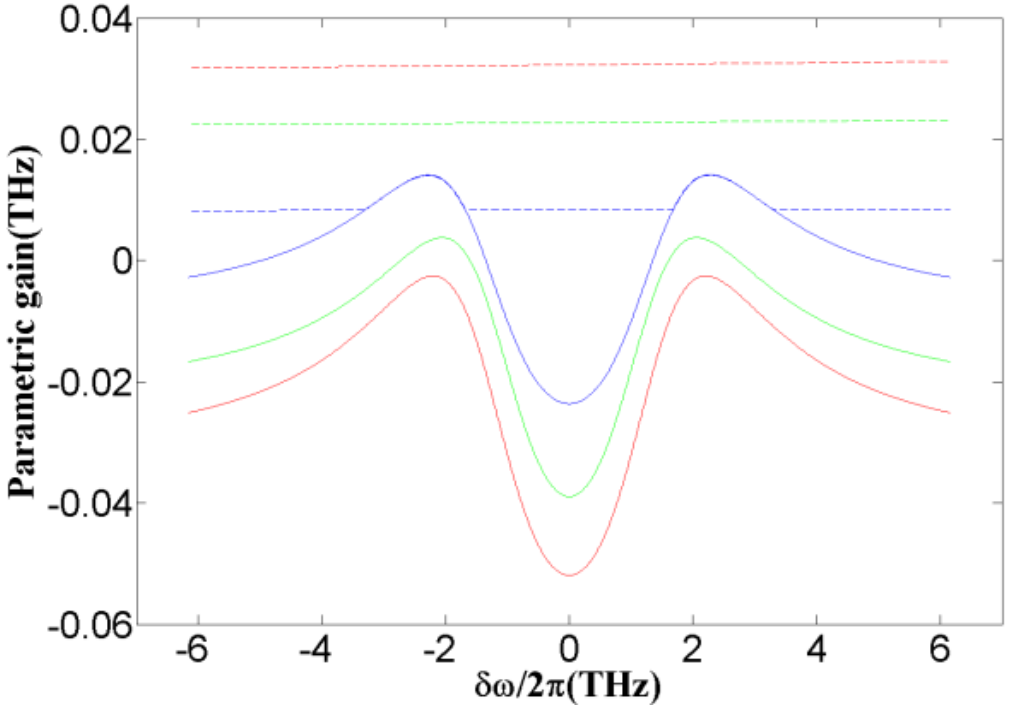

Fig. (2-2B). $p_r = 3$.

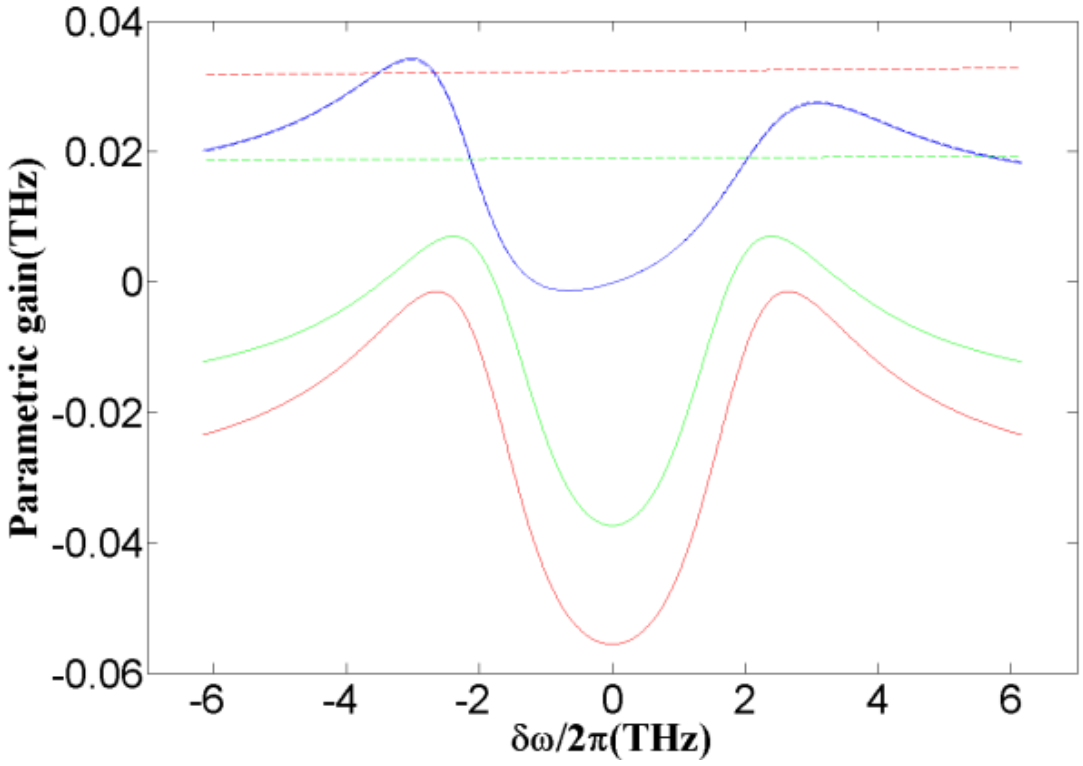

Fig. (2-2C). $p_r = 4$.

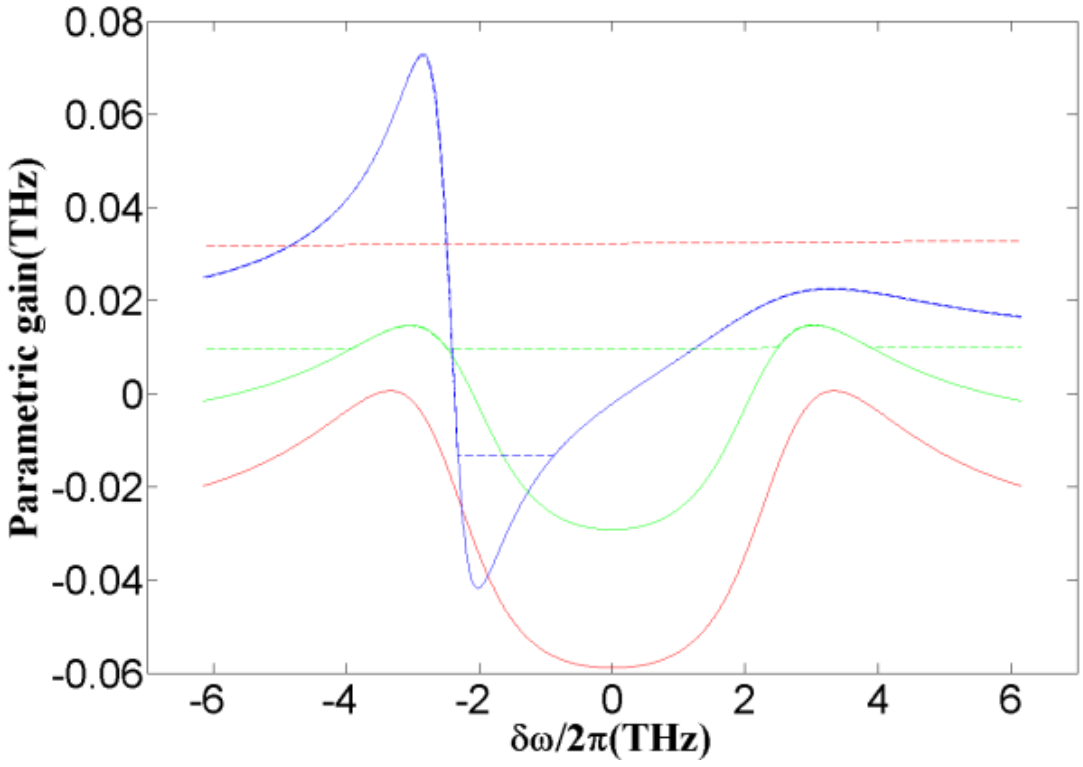

Fig. (2-2D). $p_r = 6$.

The $\delta\omega/2\pi$ represents different modes and the parametric gains in respect of detuning frequency indicate the stability of the system. Cases that GVD or saturable absorber is absent, i.e., $\beta_2 = 0$ or $\gamma = 0$ are also presented for reference. In the actual simulation, stability behaviors with β_2 varied from -10×10^{-6} ps^2/μm to -1×10^{-6} ps^2/μm are very close, so we only present the cases with $\beta_2 = -4.6 \times 10^{-6}$ ps^2/μm to show the effect of GVD.

The instability without GVD acts as a RNGH-like instability, with the agreement of the results in [23] (Fig. 1). In this case the saturable absorber is found to enhance the instability with larger value since the instability threshold is lower. However when GVD effect exists, larger saturable absorber coefficient value appear to make the system more stable. In the other words, the lasing cavity with a stronger saturable absorber effect is less affected by the presence of GVD [28].

Pumping strength p_r also affects the stability significantly. Fig. (2-2A) shows that when pumping strength is low, GVD effect turns out to flat the curve and make system unstable. While under the higher pumping strengths as shown in Fig. (2-2B), (2-2C), (2-2D), the instability with GVD is getting closer to that without GVD, which means the GVD effect is suppressed by saturable absorber effect. Since the saturable absorber effect is described by the term $\hat{\gamma}|\overline{E}|^2$, with the same saturable absorber value, it takes higher pumping strength to obtain this sort of suppression. And in Fig. (2-2C), (2-2D), the curves with $\gamma = 2\gamma_0$ become no longer symmetric. It is because of the emergence of and imaginary part in the steady-state solution [28].

CHARPER 3

Numerical Simulation on Pulse Progression of Ring-QCLs Based on Stability Analysis

In this chapter, we will present the simulation performed to study the pulse progression along the ring QCL cavity with GVD and saturable absorber effect included. The simulation model is built based on the finite-difference time-domain (FDTD) method. However the fundamental FDTD is very inefficient in QCL dynamic equations containing the GVD term, which is a second-order derivative of the propagating electric field. Thus we adopted the split-step finite difference (SSFD) method to obtain stable results.

3.1 Background

3.1.1 Finite-difference Time-domain Method

The finite-difference time-domain (FDTD) method is widely used in solving problems of electromagnetics describing by Maxwell's equations. Compared to other methods, FDTD method is simple in concept and implementation. It employs finite differences as approximations to both spatial and temporal derivatives in Maxwell's equations, providing numerical solutions to complicated problems. For instance, consider the Taylor expansions of function $f(x)$ expanded about the point x_0 with an offset of $\pm\Delta/2$:

$$f\left(x_0+\frac{\Delta}{2}\right)=f(x_0)+\frac{\Delta}{2}f'(x_0)+\frac{1}{2!}\left(\frac{\Delta}{2}\right)^2 f''(x_0)+\frac{1}{3!}\left(\frac{\Delta}{2}\right)^3 f'''(x_0)+\ldots \quad (3\text{-}1)$$

$$f\left(x_0-\frac{\Delta}{2}\right)=f(x_0)-\frac{\Delta}{2}f'(x_0)+\frac{1}{2!}\left(\frac{\Delta}{2}\right)^2 f''(x_0)-\frac{1}{3!}\left(\frac{\Delta}{2}\right)^3 f'''(x_0)+\ldots \quad (3\text{-}2)$$

where primes denote the differentiation order. Subtracting Eq. (3-2) from Eq. (3-1) yields

$$f\left(x_0+\frac{\Delta}{2}\right)-f\left(x_0-\frac{\Delta}{2}\right)=\Delta f'(x_0)+\frac{2}{3!}\left(\frac{\Delta}{2}\right)^3 f'''(x_0)+\ldots \quad (3\text{-}3)$$

Dividing by Δ on both sides leads to

$$\frac{f\left(x_0+\frac{\Delta}{2}\right)-f\left(x_0-\frac{\Delta}{2}\right)}{\Delta}=f'(x_0)+\frac{1}{3!}\left(\frac{\Delta}{2}\right)^2 f'''(x_0)+\ldots \quad (3\text{-}4)$$

The second term on the right side is depending on Δ^2, and the following terms start from Δ^4, which turn out to be even higher order. Thus Eq. (3-4) can be written as

$$f'(x_0)=\frac{f\left(x_0+\frac{\Delta}{2}\right)-f\left(x_0-\frac{\Delta}{2}\right)}{\Delta}+O(\Delta^2) \quad (3\text{-}5)$$

where the big O term represents the sum of all the terms from the order Δ^2 in Eq. (3-4), Δ^2 indicates the lowest order. If Δ is small enough, a reasonable approximation is to neglect all the terms represented by the big O. Thus the difference can be approximated by

$$f'(x_0)=\frac{f\left(x_0+\frac{\Delta}{2}\right)-f\left(x_0-\frac{\Delta}{2}\right)}{\Delta} \quad (3\text{-}6)$$

Eq. (3-6) is also called central difference approximation. Similar procedures produce forward difference approximation

$$f'(x_0) = \frac{f(x_0 + \Delta) - f(x_0)}{\Delta} \tag{3-7}$$

and backward difference approximation

$$f'(x_0) = \frac{f(x_0) - f(x_0 - \Delta)}{\Delta} \tag{3-8}$$

The approximations above provide a second order accuracy since the neglected part is on the order of Δ^2. If Δ that is used becomes smaller, the error of approximation becomes smaller as well. Dividing the temporal and spatial domain into grids with a unit of Δ, one can calculate the solution on discrete points by iteration. This also implies that if smaller Δ is chosen to obtain more accurate results, meanwhile the work of computation will increase significantly, i.e. it may take a huge amount of storage and time. Thus one has to choose an appropriate Δ. Because Δ cannot be 0, it is possible that these approximations are unstable in some cases.

3.1.2 Split-step Finite Difference (SSFD) method

One can also derive approximations of high order differences using finite-difference method, for example the GVD term in Eq. (2-6). However the numerical simulation is no longer stable in this case. To solve this problem we employ a method called split-step method, which is combined together with FDTD method as split-step finite difference (SSFD) method.

SSFD method works as follows:

Consider the nonlinear Schrödinger (NLS) equation

$$i\psi_t + \alpha(t)\psi_{xx} + v(x)\psi + \beta(t)|\psi|^2\psi = 0 \tag{3-9}$$

with the initial condition $\psi(x,0) = \psi^0(x), \quad x \in R$.

We first split Eq. (3-9) into a linear equation [30]

$$\frac{\partial \psi}{\partial t} = i\alpha(t)\frac{\partial^2 \psi}{\partial x^2} \tag{3-10}$$

and a nonlinear equation

$$\frac{\partial \psi}{\partial t} = iv(x)\psi + i\beta(t)|\psi|^2 \psi \tag{3-11}$$

Suppose the linear equation (3-10) has initial condition

$$\psi(x,0) = \psi^0(x), \quad x \in [a,b] \tag{3-12}$$

and boundary condition

$$\psi(a,t) = \psi(b,t) = 0, \quad t \in [0,T] \tag{3-13}$$

We then divide the time and space to grids with coordinates $x_j = a + jh, \quad j = 0(1)M$ and $t_n = nk, \quad n = 0,1,2...,N$, where $h = \frac{b-a}{M}$ and $k = \frac{T}{N}$ are the space and time grid step sizes, respectively. Let ψ_j^n represent the approximation of $\psi(x_j, t_n)$ and α^n represent $\alpha(t_n)$.

After approximating the space derivative in Eq. (3-10) with the fourth-order accurate compact finite difference and apply the Crank-Nicolson method, according to Reference [30], we have the following difference form

$$(A - i\gamma B)\psi^{n+1} = (A + i\gamma B)\psi^n \tag{3-14}$$

where $\gamma = 3\frac{k}{h^2}(\alpha^{n+1} + \alpha^n)$, $\psi = [\psi_1, \psi_2, ..., \psi_{M-1}]^T$, and

$$A = \begin{bmatrix} 10 & 1 & & \\ 1 & \ddots & \ddots & \\ & \ddots & \ddots & 1 \\ & & 1 & 10 \end{bmatrix}, \qquad B = \begin{bmatrix} -2 & 1 & & \\ 1 & \ddots & \ddots & \\ & \ddots & \ddots & 1 \\ & & 1 & -2 \end{bmatrix}.$$

A and B have the size of $M \times N$, $\ddots$ indicates same values with top left.

Then we use the following algorithm to approximate the solution of Eq. (3-9):

For $n = 0,1,2,....,N-1$

Step 1: for $j = 0(1)M$, approximating Eq. (3-11) produces

$$\psi_j^* = \exp\left[i/2\left(v(x_j) + \left|\psi_j^n\right|^2 \int_{t_n}^{t_{n+1}} \beta(t)dt \right)\right]\psi_j^n \tag{3-15}$$

Setp 2: for $j = 1(1)M-1$, using Eq. (3-14) and Eq. (3-15) as

$$(A - i\gamma B)\psi^{**} = (A + i\gamma B)\psi^* \tag{3-16}$$

ψ^{**} is the approximation of Eq. (3-10), can be solved from Eq. (3-16).

Step 2: for $j = 0(1)M$, approximate Eq. (3-9) using ψ^{**}

$$\psi_j^{n+1} = \exp\left[i/2\left(v(x_j) + \left|\psi_j^{**}\right|^2 \int_{t_n}^{t_{n+1}} \beta(t)dt \right)\right]\psi_j^{**} \tag{3-17}$$

SSFD method provides an alternative numerical solution for equations with high order differentiation involved, which simple finite difference methods may lead to unstable results. Its computational consume is high through, since the matrices A and B will be considerably large.

3.2 Split-step Finite Difference Simulation of Ring-QCLs with GVD

Here we describe the numerical treatment of dynamic equations of ring-QCLs using SSFD combined with FDTD. The group of dynamic equations is described in Eq. (2-6)-(2-8).

Following the split-step method in 3.1.2, we can split Eq. (2-6) to a linear equation

$$\frac{\partial E}{\partial t} = -\frac{c}{2n} i\beta_2 \frac{\partial^2 E}{\partial t^2} \tag{3-18}$$

and a nonlinear equation

$$\frac{\partial E}{\partial t} = \frac{c}{n}\left[-\frac{\partial E}{\partial z} - P - \frac{1}{2}(l_0 - \hat{\gamma} \mid E \mid^2)E \right] \tag{3-19}$$

Then the algorithm is as follows:

Step 1: solve Eq. (3-20)-(3-22), obtain the electrical field E^{∇}.

$$\frac{\partial E}{\partial t} = \frac{c}{n}\left[-\frac{\partial E}{\partial z} - P - \frac{1}{2}(l_0 - \hat{\gamma} \mid E \mid^2)E \right] \tag{3-20}$$

$$\frac{\partial P}{\partial t} = -\frac{1}{2}\sigma E - \frac{P}{T_2} \tag{3-21}$$

$$\frac{\partial \sigma}{\partial t} = \frac{l_0 p_r}{T_1 T_2} - \frac{\sigma}{T_1} + (E * P + EP * + c.c.) \tag{3-22}$$

Step 2: calculate electrical field $E^{\nabla\nabla}$ using E^{∇} and Eq. (3-23)-(3-25).

$$\frac{\partial E}{\partial t} = -\frac{c}{2n} i\beta_2 \frac{\partial^2 E}{\partial t^2} \tag{3-23}$$

$$\frac{\partial P}{\partial t} = -\frac{1}{2}\sigma E - \frac{P}{T_2} \tag{3-24}$$

$$\frac{\partial \sigma}{\partial t} = \frac{l_0 p_r}{T_1 T_2} - \frac{\sigma}{T_1} + (E * P + EP * + c.c.) \tag{3-25}$$

Step 3: calculate final solution using $E^{\nabla\nabla}$ and Eq. (3-20)-(3-22).

In the above steps, step 1 and 3 can be done in the same form, and step 2 is similar to Eq. (3-14). We need to first demonstrate the approximation for Eq. (3-20)-(3-22), then the following steps become simple.

Suppose z denotes the space, and t denotes time, the z-t plane is dived with step sizes of Δz and Δt. To get the stable difference of Eq. (3-20)-(3-22), we have chosen $\Delta z = \frac{c}{n}\Delta t$ and the derivatives as follows [20]:

$$\frac{\partial E(m,n)}{\partial t} = \frac{E(m,n+1) - E(m,n)}{\Delta t} - \frac{1}{2}\Delta t \frac{\partial^2 E(m,n)}{\partial t^2} \tag{3-26}$$

$$\frac{\partial E(m,n)}{\partial z} = \frac{E(m,n) - E(m-1,n)}{\Delta z} + \frac{1}{2}\Delta z \frac{\partial^2 E(m,n)}{\partial z^2} \tag{3-27}$$

with the same expressions for $\partial P(m,n)/\partial t$ and $\partial E(m,n)/\partial t$.

The second derivatives are calculated by differentiating Eq. (3-20) once and substituting the first-order difference approximation from Eq. (3-26) and (3-27). Then adding the two equations and transforming $\partial^2 E(m,n)/\partial t^2 - (c/n)^2[\partial^2 E(m,n)/\partial z^2]$ into first order approximation yield the following difference approximation:

$$E(m,n+1) = c_1 E(m-1,n) + c_2 P(m,n) + c_3 E(m,n) + c_4 \sigma(m,n) E(m,n) + c_5 P(m-1,n) \tag{3-28}$$

where

$$\begin{aligned} c_1 &= 1 - k\Delta t \\ c_2 &= -\frac{k}{l_0}\Delta t + \frac{k}{l_0}(\Delta t)^2\left(\frac{1}{T_2} + k\right) \\ c_3 &= \frac{1}{2}(k\Delta t)^2 \\ c_4 &= \frac{k}{2l_0}(\Delta t)^2 \\ c_5 &= -\frac{k}{l_0}\Delta t \end{aligned} \tag{3-29}$$

with

$$k = \frac{c}{2n}\left(l_0 - 2\gamma \frac{\hbar^2}{\mu^2}\frac{p_r - 1}{T_1 T_2}|E|^2\right) \tag{3-30}$$

Above E represents E(m, n). The parameters used in Eq. (3-30) can be found in Chapter 2. With similar procedures the finite difference approximation for Eq. (3-21) is given by

$$\begin{aligned} P(m,n+1) = {} & a_1 P(m,n) + a_2 E(m,n) + a_3 \sigma(m,n) E(m,n) + a_4 \sigma(m,n) E(m-1,n) \\ & + a_5 P(m,n)[E(m,n)]^2 + a_6 \sigma(m,n) P(m,n) \end{aligned} \tag{3-31}$$

where

$$
\begin{aligned}
a_1 &= 1-\frac{\Delta t}{T_2}+\frac{1}{2}(\frac{\Delta t}{T_2})^2 \\
a_2 &= -\frac{l_0 p_r}{4T_1T_2}(\Delta t)^2 \\
a_3 &= -\frac{\Delta t}{4}\left[1-\left(\frac{1}{T_1}+\frac{1}{T_2}+k\right)\Delta t\right] \\
a_4 &= -\frac{\Delta t}{4} \\
a_5 &= -\frac{(\Delta t)^2}{4} \\
a_6 &= \frac{1}{2}\frac{k}{l_0}(\Delta t)^2
\end{aligned}
\tag{3-32}
$$

And the difference approximation for Eq. (3-22) is

$$
\begin{aligned}
\sigma(m,n+1) = {} & b_1\sigma(m,n)+b_2P(m,n)E(m,n)+b_3[P(m,n)]^2+b_4P(m,n)E(m-1,n) \\
& +b_5\sigma(m,n)[E(m,n)]^2+b_6
\end{aligned}
\tag{3-33}
$$

where

$$
\begin{aligned}
b_1 &= 1-\frac{\Delta t}{T_1}+\frac{1}{2}\left(\frac{\Delta t}{T_1}\right)^2 \\
b_2 &= \frac{1}{2}\Delta t-\frac{1}{2}\left(\frac{1}{T_1}+\frac{1}{T_2}+k\right)(\Delta t)^2 \\
b_3 &= -\frac{k}{l_0}(\Delta t)^2 \\
b_4 &= \frac{1}{2}\Delta t \\
b_5 &= -\frac{1}{4}(\Delta t)^2 \\
b_6 &= \frac{l_0 p_r}{T_1T_2}\Delta t\left(1-\frac{\Delta t}{2T_1}\right)
\end{aligned}
\tag{3-34}
$$

After obtain the above expressions of approximation, we are able to calculate the solution (E^{∇}) of Eq. (3-20)-(3-22) through iteration, with some proper initial conditions of E , P , and σ . The initial conditions we have chosen are $E(x,0)=\exp(-a(x/L-0.5)^2)$, where a is a constant that may vary depending on

the actual simulation process, and $P(x,0)=0$, $\sigma(x,0)=p_r$. Since the laser cavity is a ring cavity, the boundary condition is given by

$$E(m+M,n)=E(m,n) \tag{3-35}$$

with similar relations for P and σ, where M equals $L/\Delta x$. The simulation is conducted with a M on the order of 1000.

Since the only thing different of Eq. (3-23) comparing to Eq. (3-10) is that the second derivative is to time, thus similar to Eq. (3-14), the calculation of E^{**} can be achieved by

$$(A-i\gamma B)E_{j+1}=(A+i\gamma B)E_j \tag{3-36}$$

A, B, γ remain the same, and $E=[E^1,E^2,...,E^{N-1}]^T$.

At last using E^{**} and doing the same iteration as in step 1 yield the final solution matrix, which accounts for both second and first order derivatives.

The SSFD method used here has the accuracy of Δt^2, because of the difference approximation form chosen in Eq. (3-26) and Eq. (3-27). With a properly selected Δt, the simulation yields stable pulses after a certain period of time. The results will be discussed in Section 3.3.

3.3 Parameters Selection Based on the Stability Analysis

In Chapter 2 we investigated the stability under various parameters such as strength of saturable absorber, GVD coefficient and pumping strength. The results can be used to determine the parameters in numerical simulations.

For example the strength of saturable absorber, γ, is found to make system more

unstable when getting larger. It is shown in Fig. (2-2A) that when pumping strength $p_r = 2$, with larger γ the parametric gain is approaching zero, which indicates a less stable system. Similar effects are also observed in Fig. (2-2B-D) under higher values of pumping strength. Thus one wants to select a γ that is non-zero but not too large, in this case we have chosen $\gamma = \gamma_0 \sim 2\gamma_0$ as our saturable absorber strength. Similarly large GVD is also leading to instable system, we have chosen $\beta_2 = \beta_0$ as our GVD coefficient. To achieve stable pulse output, we need to select proper combinations of GVD, saturable absorber and pumping strength. Figure (2-2A-D) also shows that the higher pumping strength the more stable modes rises with the GVD effect. So for the cases with GVD effect ($\beta_2 = \beta_0$), we selected higher pumping strength ($p_r \geq 4.7$). All parameters used in numerical simulations are listed in Table 3-1.

Quantity	**Symbol**	**Value**
Saturable absorber strength	γ	10^{-9}~2×10^{-9}cm/V^2
GVD coefficient	β_2	-4.6 × 10^{-6} ps^2/μm
Pumping strength	p_r	4.7~5.2
Gain recovery time	T_1	0.5 ps
Dephasing time	T_2	0.067 ps
Linear cavity loss	l_0	7 cm^{-1}
Transition dipole element	μ	2.54 nm×e
Background refractive index	n	3.25
Cavity length	L	6 mm

Table 3-1. The parameters used in numerical simulations.

3.4 Results and Discussions

The linear stability analysis in Chapter 2 provides the prediction of the stability, thus to obtain stable results the parameters can be adjusted according to the stability analysis. We present the logarithm scale optical intensity in frequency domain in Fig. 3-1. It is based on the Fourier transform of the stable time-domain electrical field intensity, and a.u. represents arbitrary unit. This illustrates the effect of SA and pumping strength without GVD effect.

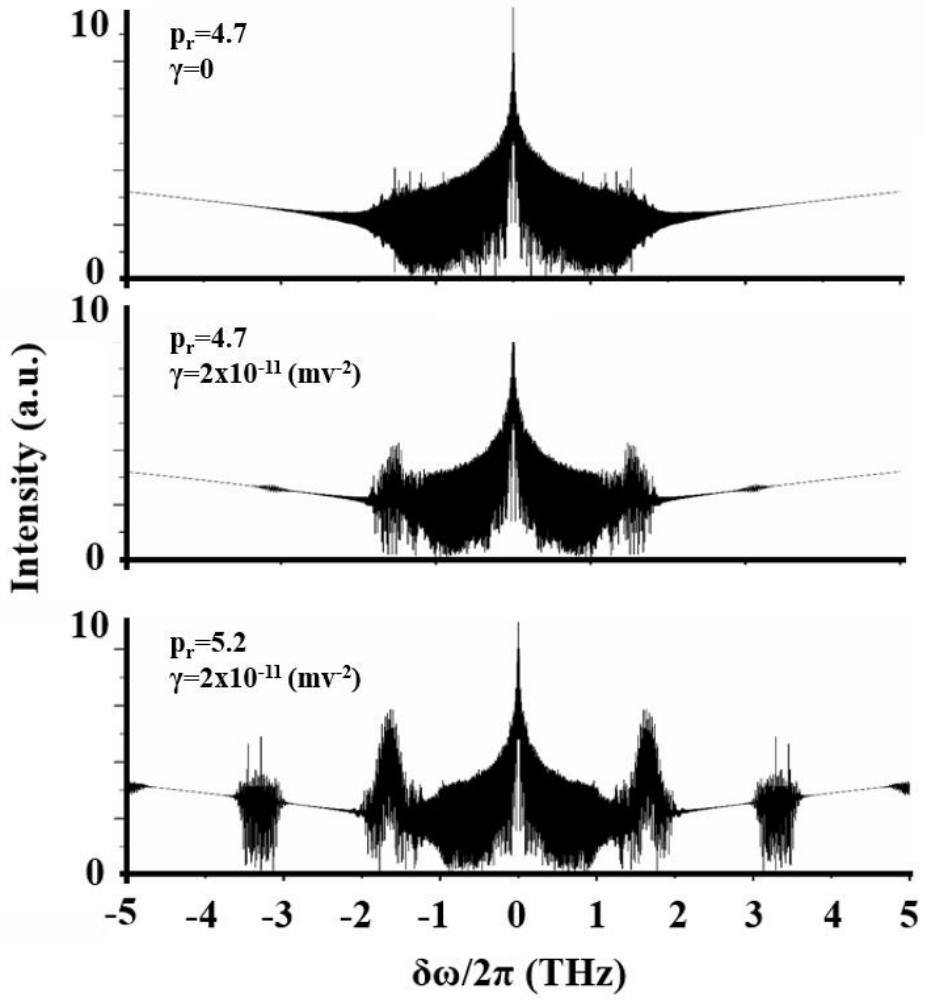

Fig. 3-1. Logarithm optical intensity with varying SA coefficients and pumping strength values.

Fig. 3-1 shows the optical spectrum consist of the central continuous-wave (CW) mode and some Rabi side modes. Under the effect of a saturable absorber, Rabi side

modes increase as shown in the second plot. Below the instability, the lasing is single-mode; when the pumping intensity is above the instability threshold, more side modes are excited and lasing becomes multi-mode. The saturable absorber effect tends to lower the threshold as presented in Chapter 2. It is also shown that Rabi sidebands around the central mode grow continuously when the threshold is exceeded. According to Ref. [31], the energy in the Rabi sidebands can change either discontinuously or continuously at the RNGH instability threshold. It could be a first or second order phase transition respectively [23]. Thus our numerical simulations indicate that such transition is on second order for QCLs including the effect of SA. Pumping strength is also found to be related to the side modes. With a larger pumping strength, more Rabi side modes appear in the spectrum as shown in Fig. 3-1, which is predicted in Ref. [32].

We also present time domain results in Fig. 3-2.

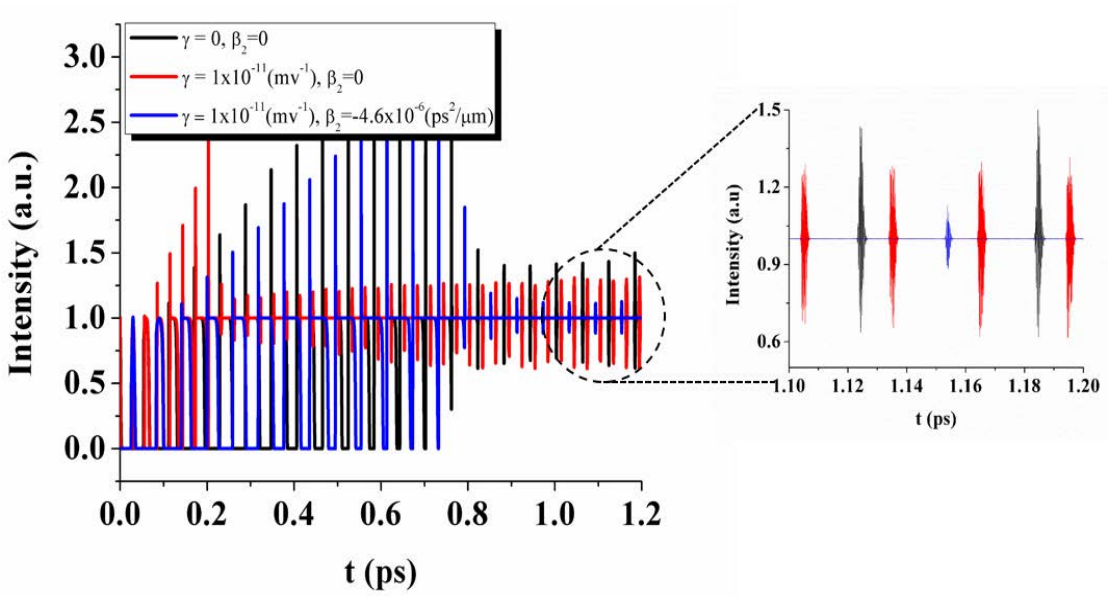

Fig. 3-2. Electrical fields inside the QCL cavity under SA effect and GVD, with zoomed out stable states.

Cases with and without GVD are shown in Fig. 3-2, the base case in which both saturable absorber and GVD are absent is used as reference. It is shown in all three cases the stable pulses are achieved at around 1 picosecond, which means these effects do not affect the time to reach stable pulses very much. Compared to the base case (without saturable absorber and GVD) and case with GVD, saturable absorber effect is found to reduce the intensity level in the cavity. Figure 3-2 shows that the intensity level with only saturable absorber starts to decrease at around 0.2 ps, which is much earlier than other cases, and it is also decreasing much faster. In contrast, after we add the GVD effect, the intensity level is changing similar to base case. This indicates that GVD effect increases the intensity level. However when the progression becomes stable, the intensity level with GVD effect is the lowest, the intensity level with saturable absorber is relatively higher, but lower than base case. And GVD effect also produces a narrower stable pulse width comparing to base case and the case with saturable absorber.

CHARPER 4

Conclusions and Future Recommendations

4.1 Conclusions

In this thesis the stability analysis and numerical simulations are demonstrated for QCLs under SA and GVD effect. The stability analysis is based on the linearization of Maxwell-Bloch equations and then eigenvalues of the Jacobian matrix of the perturbation equations describe the instability of QCL system. It is shown that the instability without GVD is a RNGH like instability and enhanced by SA effect. However when GVD is involved SA tends to make the system more stable. Pumping strength is also found to affect the instability significantly. The numerical simulations are conducted employing SSFD method, which split the equations to nonlinear part and linear part then obtain final results through three steps that combined these two parts. Simulation results show that the Rabi side modes are affected by SA effect and pumping strength. GVD lowers the intensity and shortens the pulse width when QCL system reaches a steady state. The research of this thesis provides us a better understanding of the behaviors of QCLs including a saturable absorber and GVD effect at both instability and dynamic point. We also employ a novel research pattern that is to investigate the instability first then conduct the numerical simulation based on the stability analysis, which is an efficient way to study the complicated intracavity effects of QCLs.

4.2 Suggestions for Future Work

Although the GVD effect is investigated in this thesis, SPM, which is another import effect in QCL dynamics, is not been accounted for. There has been some research on SPM in QCLs, for example Ref. [25] found that SPM could broaden the unstable domain of the RNGH instability significantly however has a trivial effect on the instability threshold. And both SA effect and SPM effects are presented in Ref. [19], where it is found that SPM effect could broaden the frequency domain of amplitude and phase instabilities, with SA effect lowering the threshold. However there has not been any research considering SA, SPM and GVD effects together in a QCL. Therefore we suggest developing the models and methods that account for these three effects in the same time to be the future research on QCLs.

APPENDIX Ⅰ: Mathematical Manipulations Producing Eq. (2-26) and Eq. (2-27)

Recall we have the Jacobian matrix

$$\begin{bmatrix} i\frac{2n}{c\beta_2} & \frac{2i}{\beta_2}\left[\frac{\partial}{\partial z}+\frac{1}{2}\left(l_0-3\hat{\gamma}\,|\,\bar{E}\,|^2\right)\right] & \frac{2i}{\beta_2} & 0 \\ 1 & 0 & 0 & 0 \\ 0 & -\frac{1}{2}\bar{\sigma} & -\frac{1}{T_2} & -\frac{1}{2}\bar{E} \\ 0 & 2\bar{P} & 2\bar{E} & -\frac{1}{T_1} \end{bmatrix} \tag{A1-1}$$

Suppose λ is any of the eigenvalues of matrix (A1-1), then λ can be calculated by the determinant of (A1-1) which is

$$\begin{vmatrix} i\frac{2n}{c\beta_2}-\lambda & \frac{2i}{\beta_2}\left[f(\lambda)+\frac{1}{2}\left(l_0-3\hat{\gamma}\,|\,\bar{E}\,|^2\right)\right] & \frac{2i}{\beta_2} & 0 \\ 1 & -\lambda & 0 & 0 \\ 0 & -\frac{1}{2}\bar{\sigma} & -\frac{1}{T_2}-\lambda & -\frac{1}{2}\bar{E} \\ 0 & 2\bar{P} & 2\bar{E} & -\frac{1}{T_1}-\lambda \end{vmatrix} = 0 \tag{A1-2}$$

Here $\frac{\partial}{\partial z}$ can replaced by $f(\lambda)$ since we suppose the derivative to z has the form of $\frac{d\delta\rho^E(z)}{dz}=f(\lambda)\delta\rho^E(z)$.

Now we have to calculate Eq. (A1-2) to get the expression of $f(\lambda)$. The determinant of a 4×4 matrix can be calculated by many ways, here we just choose a form that employs cofactors:

$$\det(A)=a_{11}\det(M_{11})-a_{12}\det(M_{12})+a_{13}\det(M_{13})-a_{14}\det(M_{14}) \tag{A1-3}$$

where M_{ij} is the minor of row i and column j.

Using Eq. (A1-3) to calculate Eq. (A1-2) yields

$$\left(i\frac{2n}{c\beta_2}-\lambda\right)\begin{vmatrix} -\lambda & 0 & 0 \\ -\frac{1}{2}\bar{\sigma} & -\frac{1}{T_2}-\lambda & -\frac{1}{2}\bar{E} \\ 2\bar{P} & 2\bar{E} & -1/T_1-\lambda \end{vmatrix}$$

$$-\frac{2i}{\beta_2}\left[f(\lambda)+\frac{1}{2}\left(l_0-3\hat{\gamma}\,|\bar{E}|^2\right)\right]\begin{vmatrix} 1 & 0 & 0 \\ 0 & -\frac{1}{T_2}-\lambda & -\frac{1}{2}\bar{E} \\ 0 & 2\bar{E} & -1/T_1-\lambda \end{vmatrix} \qquad \text{(A1-4)}$$

$$+\frac{2i}{\beta_2}\begin{vmatrix} 1 & -\lambda & 0 \\ 0 & -\frac{1}{2}\bar{\sigma} & -\frac{1}{2}\bar{E} \\ 0 & 2\bar{P} & -1/T_1-\lambda \end{vmatrix} = 0$$

The determinants of the 3×3 matrices are easy to calculate. We have

$$\left(i\frac{2n}{c\beta_2}-\lambda\right)\left[\left(-\frac{1}{T_2}-\lambda\right)\left(-\frac{1}{T_1}-\lambda\right)+\bar{E}^2\right]$$
$$-\frac{2i}{\beta_2}\left[f(\lambda)+\frac{1}{2}\left(l_0-3\hat{\gamma}\,|\bar{E}|^2\right)\right]\left[\left(-\frac{1}{T_2}-\lambda\right)\left(-\frac{1}{T_1}-\lambda\right)+\bar{E}^2\right] \qquad \text{(A1-5)}$$
$$+\frac{2i}{\beta_2}\left[\left(-\frac{1}{2}\bar{\sigma}\right)\left(-\frac{1}{T_1}-\lambda\right)+\bar{P}\bar{E}\right]=0$$

Moving all the terms to the right side other than $f(\lambda)$, we obtain the expression

$$f(\lambda)=-i\frac{\beta_2}{2}\lambda^2-\frac{n}{c}\lambda-\frac{1}{2}\left(l_0-3\hat{\gamma}\,|\bar{E}|^2\right)+\frac{\bar{\sigma}T_2+2\bar{P}\bar{E}T_1T_2}{2\left[\left(T_1+\lambda T_1T_2\right)\left(T_2+\lambda T_1T_2\right)+\bar{E}^2T_1T_2\right]} \qquad \text{(A1-5)}$$

According to Eq. (2-30) $f(\lambda_k)=j\frac{2\pi k}{L}$, λ_k can be calculated by solving the polynomial equation. Plotting the eigenvalues to different k yields the results of stability analysis.

APPENDIX Ⅱ: Transformation of the Second-order Difference in Approximation to Eq. (3-20)

Recall we have the second-order difference $\partial^2 E(m,n)/\partial t^2 - (c/n)^2[\partial^2 E(m,n)/\partial z^2]$ in the approximation to Eq. (3-20), this can be transformed to first-order difference as follows:

Do the derivative of t to Eq. (3-20), we have

$$\frac{\partial^2 E}{\partial t^2} = \frac{c}{n}\left[-\frac{\partial^2 E}{\partial z \partial t} - \frac{\partial P}{\partial t} - \frac{1}{2}(l_0 - 3\hat{\gamma}\,|E|^2)\frac{\partial E}{\partial t}\right] \tag{A2-1}$$

Then do the derivative of z to Eq. (3-20), we obtain

$$\frac{\partial^2 E}{\partial z \partial t} = \frac{c}{n}\left[-\frac{\partial^2 E}{\partial z^2} - \frac{\partial P}{\partial z} - \frac{1}{2}(l_0 - 3\hat{\gamma}\,|E|^2)\frac{\partial E}{\partial z}\right] \tag{A2-2}$$

Substituting (A2-2) to (A2-1) yields

$$\frac{\partial^2 E}{\partial t^2} = \frac{c}{n}\left[\frac{c}{n}\left[\frac{\partial^2 E}{\partial z^2} + \frac{\partial P}{\partial z} + \frac{1}{2}(l_0 - 3\hat{\gamma}\,|E|^2)\frac{\partial E}{\partial z}\right] - \frac{\partial P}{\partial t} - \frac{1}{2}(l_0 - 3\hat{\gamma}\,|E|^2)\frac{\partial E}{\partial t}\right] \tag{A2-3}$$

Finally we have the expression

$$\frac{\partial^2 E}{\partial t^2} - \left(\frac{c}{n}\right)^2 \frac{\partial^2 E}{\partial z^2} = \frac{c}{n}\left[\frac{c}{n}\left[\frac{\partial P}{\partial z} + \frac{1}{2}(l_0 - 3\hat{\gamma}\,|E|^2)\frac{\partial E}{\partial z}\right] - \frac{\partial P}{\partial t} - \frac{1}{2}(l_0 - 3\hat{\gamma}\,|E|^2)\frac{\partial E}{\partial t}\right] \tag{A2-4}$$

The right side only contains first-order derivative that can be either found in Eq. (2-20) to (2-22), or replaced by the finite difference approximation. After approximating all the first-order difference we can obtain the final approximation form of Eq. (2-20).

References

1. J. Faist, F. Capasso, D. L. Sivco, A. L. Hutchinson, and A. Y. Cho, “Quantum cascade laser”, Science 64, 553-556 (1994).
2. Y. Yao et al., “Mid-infrared quantum cascade laser”, Nature Photonics, July 2012, Vol. 6(7), pp.432-439.
3. F. Xie et al., “Room temperature CW operation of short wavelength quantum cascade lasers made of strain balanced GaxIn1−xAs/AlyIn1−yAs material on InP substrates”, IEEE Journal on Selected Topics in Quantum Electronics, 2011, Vol.17(5), pp.1445-1452.
4. O. Fedosenko et al., “InP-based mid-infrared quantum-cascade laser grown on pre-patterned wafer”, Journal of Crystal Growth, 15 May 2011, Vol. 323(1), pp.488-490.
5. D. G. Revin et al., “InP-Based mid-infrared quantum cascade lasers for wavelengths below 4 μm”, IEEE Journal on Selected Topics in Quantum Electronics, 2011, Vol. 17(5), pp.1417-1425.
6. N. Lang et al., “In situ monitoring of plasma etch processes with a quantum cascade laser arrangement in semiconductor industrial environment”, Journal of Physics: Conference Series, 2009, Vol.157.
7. C. Sirtori et al., “GaAs–AlGaAs quantum cascade lasers: physics, technology, and prospects”, IEEE Journal of Quantum Electronics, Vol. 38, No. 6, June 2002.
8. T. Kruczek et al., “InAs/AlSb widely tunable external cavity quantum cascade laser around 3.2 μm”, Applied Physics Letters, 7 January 2013, Vol. 102(1).
9. J. Bai and D. S. Citrin, “Intracavity nonlinearities in quantum-cascade lasers”, J. Appl. Phys. 106, 031101 (2009).
10. F.Capasso, C. Gmachl, D. L. Sivco and A. Y. Cho, Phys. Today 55(5), 34 (2002).
11. A. Y. Cho, J. Crystal Growth 111, 1 (1991).
12. A. Lyakh et al., “1.6 W high wall plug efficiency, continuous-wave room temperature quantum cascade laser emitting at 4.6 μm”, Applied Physics Letters

92, 111110 (2008).

13. X. J. Wang et al., “High power ~ 6.14um quantum cascade laser by MOCVD”, Conference Proceedings - Lasers and Electro-Optics Society Annual Meeting-LEOS, 2008, pp.753-754
14. J. C. Shin et al., “Characteristics of mid-IR-emitting deep-well quantum cascade lasers grown”, J. of Crystal Growth, 1 April 2010, Vol. 312(8), pp.1379-1382.
15. O. Malis et al., “The Quantum Cascade Laser: A Versatile High-Power Semiconductor Laser for Mid-Infrared Applications”, Bell System Technical Journal, 2005, Vol. 10(3), pp.199-214.
16. C. Gmachl, F. Capasso, D. L. Sivco, and A. Y. Cho, “Recent Progress in Quantum Cascade Lasers and Applications,” Rep. Prog. Phys., 64 (2001), 1533–1601.
17. G. P. Agrawal, Nonlinear Fiber Optics, 3rd ed., Academic Press, San Diego, California (2001).
18. R. Paiella et al,. “Self-mode-locking of quantum cascade lasers with giant ultrafast optical nonlinearities”, Science 290, 1739-1742 (2000).
19. J. Bai, “Phase instability and amplitude instability of quantum-cascade lasers with Fabry-Perot cavity”, IEEE Trans. Nanotechnol. 11, 292-297 (2012).
20. H. Risken, K. Nummedal, “Self-pulsing in lasers” J. Appl. Phys. 39, 4662 (1968).
21. Graham and H. Haken, “Quantum theory of light propagation in a fluctuating laser-active medium”, Zeitschrift für Physik A, vol. 213, no. 5, pp. 420-450, 1968.
22. C. Y. Wang et al., “Coherent instabilities in a semiconductor laser with fast gain recovery”, Phys. Rev. A, 75, 031802 (2007).
23. A. Gordon et al., “Multimode regimes in quantum cascade lasers: from coherent instabilities to spatial hole burning”, Phys. Rev. A 77, 053804 (2008).
24. G. P. Agrawal et al., “Effect of Gain Dispersion on Ultrashort Pulse Amplification in Semiconductor Laser Amplifiers”, IEEE Journal of Quantum Electronics, June 1991, Vol. 27(6), pp.1843-1849.
25. J. Bai, “Effect of self-phase modulation on the instabilities of quantum-cascade lasers”, J. Nanophoton. 4(1), 043519 (October 29, 2010).

26. H. Choi et al., “Time domain upconversion measurements of group-velocity dispersion in quantum-cascade lasers”, Opt. Express 15, 15898-15907 (2007)
27. M. A. Talukder, and C. R. Menyuk, “Self-induced transparency modelocking of quantum-cascade lasers in the presence of saturable nonlinearity and group velocity dispersion”, Opt. Express 18, 5639-5653 (2010).
28. J. Bai, and D. Zhou, “Effect of group-velocity dispersion on the stability of quantum-cascade lasers”, J. Nanophoton. 7, 073079 (2013).
29. J. Ohtsubo, “Semiconductor Lasers: Stability, Instability and Chaos”, Berlin, New York, Springer Verlag 2008.
30. M. Dehghan, and A. Taleei, “A compact split-step finite difference method for solving the nonlinear Schrodinger equations with constant and variable coefficients”, Comp. Phys. Commun. 181, 43-51 (2010).
31. H. Haken, and H. Ohno, “Onset of ultrashort laser pulses: First or second order phase transition”, Opt. Commun. 26, 117-118 (1978).
32. M. Moradinasab, M. Pourfath, O. Baumgartner, and H. Kosina, “Performance optimization and instability study in ring cavity quantum cascade lasers”, ITQW13, Bolton Landing, NY (2013).